



Interaction between the Ekman layer and the Couette–Taylor instability

V. Sobolík^a, B. Izrar^{b,*}, F. Lusseyran^c, S. Skali^c

^a*Institute of Chemical Process Fundamentals, AS CR, 16502 Prague 6, Czech Republic*

^b*Laboratoire d'Aérodynamique, CNRS UPR 9020, 1C Avenue de la Recherche Scientifique, 45067 Orléans Cedex 2, France*

^c*LEMTA–CNRS–UMR 7563, 2 Avenue de la Forêt de Haye, B.P. 160, 54504 Vandoeuvre les Nancy, France*

Received 28 July 1999; received in revised form 18 February 2000

Abstract

The finite aspect ratio effect on Couette–Taylor flow was studied by means of three-segment electrodiffusion probes. The geometry of the Couette apparatus was characterized by the cylinders radii $R_1 = 100$ mm and $R_2 = 110$ mm and by the aspect ratio $\Gamma = L/(R_2 - R_1) = 9.85$. The velocity gradient components were measured by electrodiffusion probes placed at the steady outer wall and at a confining ring between cylinders. The distributions of the azimuthal and axial components of velocity gradient at the outer wall indicated the existence of Ekman vortices at rotation rates smaller than the critical rate of onset of Taylor vortices in an infinitely long gap. The amplitude of the azimuthal component of velocity gradient of Ekman vortex grows linearly with Taylor number. The results of measurements are in good agreement with numerical simulations made by a finite element method which in turn gives a complete description of the flow. © 2000 Elsevier Science Ltd. All rights reserved.

1. Introduction

The flow between concentric rotating cylinders has been intensively studied in the last three decades both theoretically and experimentally [1]. When the rotation rate of the inner cylinder exceeds a critical value, Ta_C , the circular shear Couette flow is replaced by a flow with steady toroidal cells — counter-rotating Taylor vortices. Further increase of the rotation rate brings about the following scenario: azimuthal waves on the toroidal roll cells at Ta_w , modulated azimuthal waves, turbulent flow in the cells and ultimately turbulent flow in the whole gap. Couette–Taylor flow with

superposed small axial flow has practical applications. Legrand and Coeuret [2] and Desmet et al. [3] studied mixing in the cells with the aim of making use of Couette–Taylor flow in chemical reactors because it exhibits a narrow residence time distribution and low velocity gradients. Kataoka et al. [4] found that regimes with modulated azimuthal waves and weakly turbulent cells are convenient for emulsion polymerization of styrene. The use of Taylor vortex flow for the control of concentration polarization and membrane fouling was reviewed by Mikulasek [5]. Dumont found structures similar to Taylor vortices in heat exchangers with scraped walls [6].

The equipments making use of Couette–Taylor flow have cylinders with finite length and are confined by rigid boundaries. This means that their aspect ratio is finite. It is well known, see Andereck et al. [7], that toroidal vortex motion starts in the

* Corresponding author. Tel.: +33-02-38-25-77-00; fax: +33-02-38-25-77-77.

E-mail address: aero@cnrs-orleans.fr (B. Izrar).

Nomenclature

F	Farraday constant		
c	concentration of active species	v	azimuthal velocity component
c_E	Emkrox concentration b.w.	$v_x = \partial v / \partial x$	gradient of azimuthal velocity component at the ring
$d = R_2 - R_1$	gap width	$v_y = \partial v / \partial y$	gradient of azimuthal velocity component at the outer wall
D	coefficient of diffusion of active species	w	axial velocity component
I	electric current	$w_y = \partial w / \partial y$	gradient of axial velocity component at outer wall
k	segment number	x	distance from fixed ring
K	multiplication parameter in dependence of current on velocity gradient	$y = R_2 - r$	distance from outer wall
L	gap length		
n	exponent in dependence of current on velocity gradient	<i>Greek symbols</i>	
n_e	number of electrons involved in reaction of one ion	μ	dynamic viscosity
R	electrode radius	ρ	density
R_1	radius of the inner cylinder	Ω	rotation rate
R_2	radius of the outer cylinder		
r, z, θ	radial, axial and azimuthal coordinate	<i>Subscripts</i>	
$Ta = \frac{\rho \Omega R_1 d}{\mu} \sqrt{\frac{d}{R_1}}$	Taylor number	C	critical value at which Taylor vortices start
u	radial velocity component	e	extreme value
$u_x = \partial u / \partial x$	gradient of radial velocity component at the ring	W	critical value at which azimuthal waves start

Ekman layers adjacent to the motionless boundaries much earlier than Taylor vortices. Although Ekman vortices are very important from a practical point of view, they have not been studied as intensively as the classical Couette–Taylor problem with an infinite aspect ratio. Benjamin [8,9] studied the mutation of primary flow as the length of comparatively short annulus was changed. Mullin [10] investigated the evolution of primary flow and the transition from N -cell mode to $(N+2)$ -cell mode by flow visualization. At small rotation rates, Mullin observed that the steady motion was mainly in circles, but some three-dimensional features may appear near the fixed end walls. At a critical rotation rate, cells grew progressively from the ends to meet at the centre forming a primary cellular flow that is uniquely determined over the respective range of aspect ratio. Cliffe [11] and Anadouli et al. [12] used finite-element methods for flow simulations in a comparatively short annulus.

The knowledge of the wall shear distribution is important for the design and optimization of the above mentioned equipment. Cognet [13] started a long series of wall velocity gradient measurements in Couette–Taylor flow. He then used simple probes for measuring the axial distribution of the limiting diffusion current.

Sobolík [14] has shown that three-segment electrodiffusion micro-probes are very convenient for mapping the axial distribution of azimuthal and axial components of the velocity gradient at the wall of the fixed outer cylinder.

The aim of the present paper is an experimental and numerical investigation of the Ekman vortices and their interaction with the Taylor vortices. Axial distribution of the azimuthal and axial components of the wall velocity gradient is measured by three-segment electrodiffusion probes at the fixed outer wall of an annulus with a comparatively small length enclosed by two fixed rings. The vortices are swept along the probes by moving the rings simultaneously in the axial direction. Another measurement is made using a three-segment probe fixed in the upper ring. The azimuthal and radial components of the wall velocity gradient at the upper ring are measured by this probe. The experimental results are compared with numerical simulations made by a finite element method.

2. Experimental conditions

The experimental apparatus, which has already been used for several other studies, e.g. by Ait Aider [15],

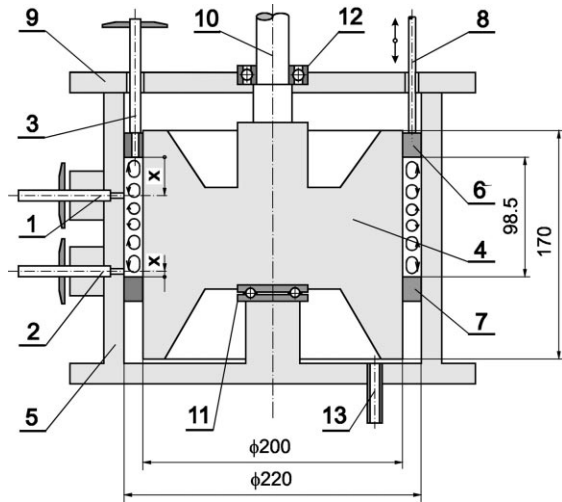


Fig. 1. Experimental apparatus: 1, 2, 3 — three-segment probes #1, #2 and #3, 4 — rotating inner cylinder, 5 — fixed outer cylinder, 6 — upper ring, 7 — lower ring, 8 — rods, 9 — cover, 10 — cylinder shaft, 11 — sunk pivot ball bearing, 12 — self-aligning ball bearing, 13 — fitting.

was modified for the present work, (Fig. 1). It consists of an inner Plexiglas cylinder with a diameter of 200 mm and a height of 170 mm and a cylindrical Plexiglas vessel with an inner diameter of 220 mm and a height of 200 mm. The cylinder is led by a sunk pivot ball bearing at the bottom and a self-aligning ball bearing in the cylinder cover. A direct current motor drives the cylinder by means of belt and pulleys. Rotation rate is adjusted manually by a potentiometer. Flow structures were confined in a cage of two fixed Plexiglas rings with an inner diameter of 201 mm and outer diameter of 219 mm and a height of 15 mm. Three stainless steel bands with a thickness of 0.3 mm and a width of

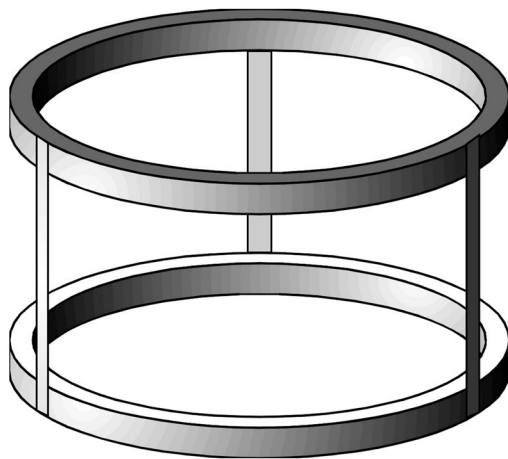


Fig. 2. Cage of the rings.

10 mm connect the two rings at the outer perimeter, (Fig. 2). The distance between the rings is 98.5 mm. The upper ring is suspended on three rods, which are moved simultaneously in the vertical direction by a central screw with a thread of 1 mm. Two three-segment electrodiffusion probes are mounted flush to the vessel wall and one probe to the upper ring. The cage displacement is limited by the liquid level. Hence the velocity gradient distribution in the upper part is measured with the upper probe and in the lower part with the lower probe. The apparatus is filled through a hose and a fitting mounted in the vessel bottom. The liquid temperature is measured by a thermometer immersed in a T-fitting on the hose.

A cylindrical system of co-ordinates r, θ, z and measured velocity gradient components are shown schematically in Fig. 3. The azimuthal component $\partial v/\partial y$ and the axial component $\partial w/\partial y$ of the velocity gradient are measured simultaneously by two three-segment probes at the wall of the outer cylinder, $r = R_2$. With the aim of obtaining the axial distribution of the velocity gradient components, the vortices are swept along the probes by a slow axial motion of the cage. When the liquid is held at the level of the upper fixed ring, the vortices follow the axial motion of the cage without any distortion. The cage is raised in steps of 1 mm. Two other components of the wall velocity gradient, $\partial v/\partial x$ and $\partial u/\partial x$, are measured by a flush mounted probe in the upper ring, $z = L$ is

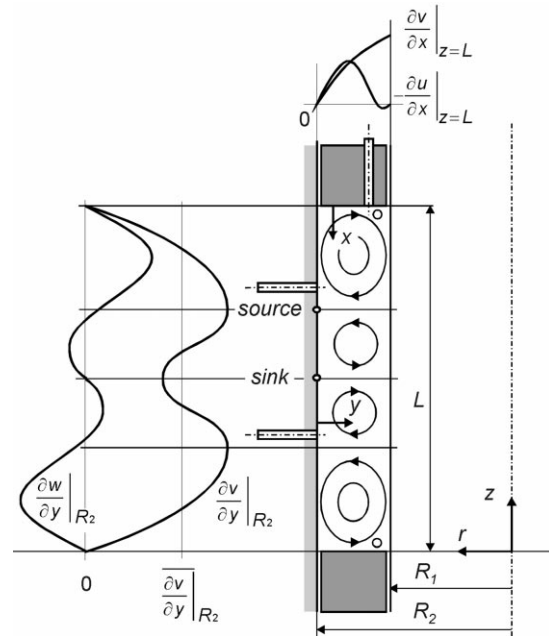


Fig. 3. Definition of measured velocity gradient components and system of co-ordinates.

flush mounted in the upper ring at a distance of 3.3 mm from the inner cylinder.

Before each series of measurements, critical rotation rates of the Taylor vortices onset, Ω_C , and of the onset of azimuthal waves on Taylor vortices, Ω_W , were estimated. For this purpose, the liquid level was lowered a few millimetres below the upper ring. Supposing that the free liquid level is a plane of symmetry, the aspect ratio was doubled in this way to a value of 19.7 that could be considered as an infinite ratio. The components of velocity gradients were then followed with the upper probe at a distance of 10 mm below the liquid surface. The Taylor vortices manifested themselves by a non-zero component $\partial w/\partial y$, and wavy flow by fluctuations of both components, $\partial w/\partial y$ and $\partial v/\partial y$.

Taylor instabilities appeared in our water filled apparatus at a wall velocity gradient of about 1.2 s^{-1} . Ekman vortices started at an even lower velocity gradient. It is possible to measure such a small gradient by three-segment electrodiffusion probes [14], but higher gradients are resolved with a better accuracy. Therefore, we have looked for a liquid with a higher viscosity in which electrodiffusion method works well. Aqueous solutions of glycerol are not very suitable, as high concentrations are necessary to increase the viscosity. The diffusivity of species in concentrated solutions of glycerol is low. On the contrary, water soluble polyalkylen glycols, mostly used as synthetic lubricants, need a much smaller concentration to achieve a high viscosity. An aqueous solution of 20% Emkarox HV 45 (product of ICI), has a viscosity of approximately $\mu = 48 \text{ mPa s}$, a density of 1050 kg m^{-3} and a diffusivity of $D = 3 \times 10^{-10} \text{ m}^2 \text{ s}^{-1}$ at a temperature of 22°C . The electrolyte does not change the viscosity very much, which is constant in the range of velocity gradients ($10, 300 \text{ s}^{-1}$) encountered in our experiments. The properties of aqueous Emkarox solutions did not change during the 3 months of experiments.

Chopin et al. [16] describe pure Emkarox as a highly elastic-constant viscosity liquid. Therefore, we verified the elasticity of aqueous solutions with the electrolyte and its influence on the Taylor instability in several ways. The complex modulus, G^* , of 22.8% Emkarox solution was measured in the Weissenberg Rheogoniometer CARRI-MED. It follows from the values of the storage modulus G' , which achieved only 13% of the loss modulus G'' in the frequency range (1, 10) Hz, that this solution is only slightly elastic. Thomas and Walters [17] showed that the elasticity decreases the critical Taylor number of Couette flow. This was not the case for the Emkarox solutions used in our experiments, because the critical Taylor number calculated from the measured viscosity and critical rotation rates did not differ more than 3% from the value $Ta_c = 43.7$, which was found for inelastic liquids

and infinite aspect ratio [18]. Another proof that the solution can be treated as purely viscous was the agreement of the measured components of the velocity gradients with the numerical simulation.

3. Three-segment electrodiffusion probes

The electrodiffusion method of wall velocity gradient evaluation is based on the measurement of the electrical current which flows through an electrolytic cell. The cell is composed of a small working electrode, a much larger auxiliary electrode and an electrolyte. The electrolytes with redox reaction are used preferably. If the reaction kinetics is fast, the voltage between electrodes is high enough and the migration effect is suppressed by supporting electrolyte, the electric current depends only on the molecular and convective diffusion processes in the vicinity of the working electrode — the probe. A plateau in the dependence of current on voltage is characteristic for this so-called limiting diffusion current, I . Polarograms shown in Fig. 4 were measured with the three-segment platinum probe #2 in 20% Emkarox with 25 mol m^{-3} potassium ferri- and ferro-cyanid and 2% K_2SO_4 . They show quite a good plateau in the interval $(-0.9, -0.2) \text{ V}$. The auxiliary electrode was a platinum sheet with dimensions $10 \times 20 \text{ mm}^2$ glued in the vessel bottom. Voltage -0.8 V was adjusted in the measurements of velocity gradients.

Neglecting the diffusion in the longitudinal and the span-wise directions relative to the homogenous flow field characterized by a wall velocity gradient, γ , the Leveque solution

$$I = 2.155n_eFcD^{2/3}R\gamma^{1/3} \quad (1)$$

is valid for a circular electrode with radius R , flush mounted into the wall. Because the concentration, c ,

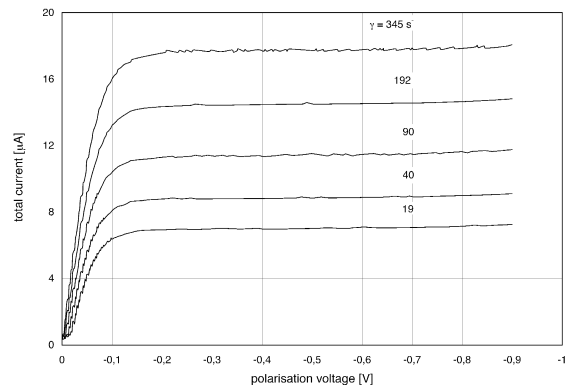


Fig. 4. Polarograms measured by three-segment probe #2 in 20% EMKAROX at several velocity gradients.

the diffusivity of species, D , and the probe geometry are not always exactly known, it is necessary to make a calibration by measuring the dependence, $I = K\gamma^n$, under well defined velocity gradients. For this purpose, a smaller radial gap was created in the apparatus (Fig. 5), by pulling two PVC rings with an outer diameter of 214 mm and a height of 30 mm on the cylinder 4 in the height of the probes 1 and 2. The annular gap of 3 mm allowed much higher velocity gradients in laminar flow than the 10 mm gap used in the experiments. The calibration results of the probe #2 in 20% Emkarox are given in Fig. 5. Due to the molecular diffusion in the longitudinal and the span-wise directions (low Peclet number) the exponent n has a smaller value than that of the Leveque solution. The values of $K = 2.862, n = 0.31$ were used for $\gamma \in (10, 200) \text{ s}^{-1}$ and $K = 2.625, n = 0.33$ for $\gamma \in (70, 500) \text{ s}^{-1}$. The parameter K was verified by the current measurement before and after each experimental run in the 10 mm gap at maximum rotation rate of the laminar Couette flow.

Eq. (1) was obtained by integrating the current density i over the electrode surface. It holds $i \approx x_e^{-1/3}$, where the distance x_e is measured from the front electrode edge in the flow direction. Distribution of the current density on a three-segment electrode is shown in Fig. 6. The shadowing is darker with the higher current density. It is clear that the rear segments have smaller current than the forward one. The theory of three-segment probes was established by Wein and Sobolik [19]. The dependence of the current through a

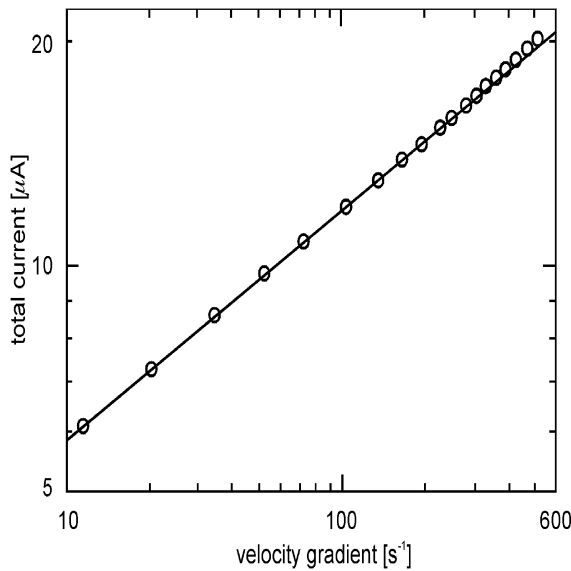


Fig. 5. Dependence of the total current of three-segment probe #2 on the velocity gradient. Full line $-I = 2.862(\partial v / \partial y)^{0.31}$.

segment, normalized by the total current, $I_j / \sum I_k$, on the flow direction was called a directional characteristic. It is necessary to measure directional characteristics of real probes, for example by turning a probe, which is flush mounted into the wall exposed to a steady laminar shear flow. The directional characteristics of the probe #2 are shown in Fig. 7. The magnitude of the velocity gradient and the flow direction were calculated and displayed on-line by means of the software [20].

Three-segment probes are circular probes composed of insulated segments (Fig. 8). The three-segment probes were fabricated in house by pulling simultaneously three platinum wires through a goldsmith wire-drawing die. The platinum wires were annealed after each pulling. In the beginning the wires had a diameter of 0.5 mm and the pulling started through a cylindrical hole with a diameter of 1 mm. Reshaped into a sector-form, the originally circular wires fulfilled totally the last die with a diameter of 0.5 mm. They were then coated electrophoretically with a deposit of a polymeric paint. They were then glued together with the Epoxy resin 1200 (United Chemical and Metallurgical Works). A small amount of the resin was put among the wires, which were then pressed tightly together by a jaw collet. After soldering leads, the wires were glued with an Epoxy resin CHS 521 (United Chemical and Metallurgical Works) into a stainless tube with a tip diameter of 3 mm and an inner diameter of 1 mm. The tube face was polished with emery paper of a grit size 15 μm. The stainless tube served as an anode and also as an electrode screening. The fabrication procedure was improved considerably during the last years; compare the probe used in the present study (Fig. 8), with the probe used earlier by Deslouis et al. [21].

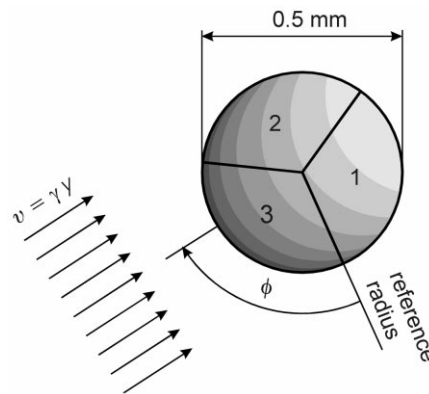


Fig. 6. Distribution of the current density on a three-segment probe.

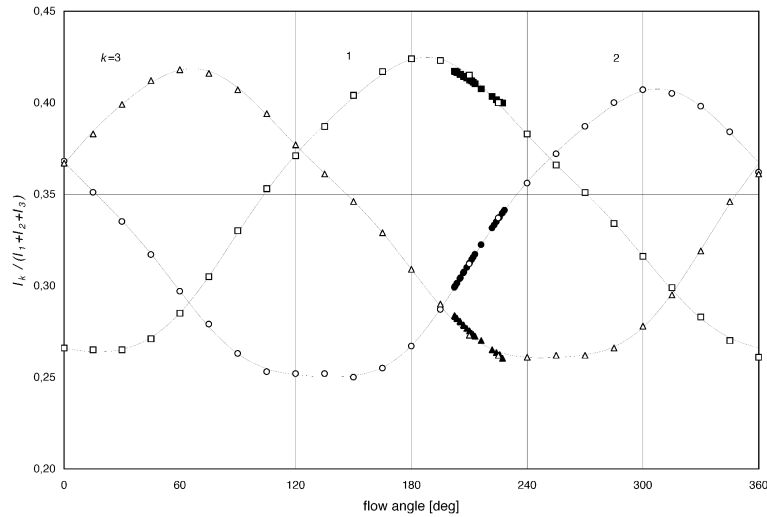


Fig. 7. Directional characteristics of three-segment probe #2. Open points were obtained by calibration, lines by fitting these points by Fourier series of fourth order and full points stand for measurement of the Ekman vortex shown in Fig. 10(c).

4. Numerical model

The Couette–Taylor flow, confined in the vertical direction, is also explored numerically. The behaviour of the end wall vortices is analysed for sub-critical and critical Taylor numbers. For a sufficiently slow rotation, the equations describing the flow are the axisymmetrical Navier–Stokes equations, i.e. three velocity components and 2 geometry variables. We introduce the non-dimensional variables using d, Ω^{-1} and ΩR_1 , respectively as length, time and velocity scales.

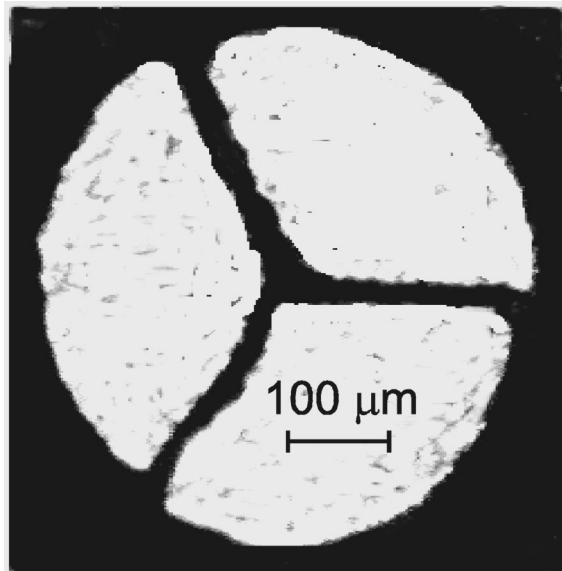


Fig. 8. Microphotograph of probe #2.

The non-dimensional system to be solved is:

$$\frac{\partial u}{\partial t} + u \frac{\partial u}{\partial r} + w \frac{\partial u}{\partial z} + \frac{v^2}{r} = -\frac{\partial p}{\partial r} + \frac{1}{Re} \left(\Delta u - \frac{u}{r^2} \right)$$

$$\frac{\partial v}{\partial t} + u \frac{\partial v}{\partial r} + w \frac{\partial v}{\partial z} - \frac{uv}{r} = \frac{1}{Re} \left(\Delta v - \frac{v}{r^2} \right)$$

$$\frac{\partial w}{\partial t} + u \frac{\partial w}{\partial r} + w \frac{\partial w}{\partial z} = -\frac{\partial p}{\partial z} + \frac{1}{Re} (\Delta w) \tag{2}$$

with

$$\Delta = \frac{\partial^2}{\partial r^2} + \frac{1}{r} \frac{\partial}{\partial r} + \frac{\partial^2}{\partial z^2}$$

and where $Re = \Omega R_1 d \rho / \mu$: Reynolds number, p : pressure, and u, v, w : the velocity components. The domain is $R_1 \leq r \leq R_2$ and $0 \leq z \leq L$.

The continuity equation is:

$$\frac{1}{r} \frac{\partial(ru)}{\partial r} + \frac{\partial w}{\partial z} = 0. \tag{3}$$

The non-slip boundary conditions are:

$$u = w = 0 \quad \text{at} \quad r = \frac{R_1}{d} \quad \text{and} \quad \frac{R_2}{d}; \quad 0 \leq z \leq \frac{L}{d}$$

$$u = v = w = 0 \quad \text{at} \quad z = 0 \quad \text{and} \quad z = \frac{L}{d}; \quad \frac{R_1}{d} \leq r \leq \frac{R_2}{d}$$

$$v = 1 \quad \text{at } r = \frac{R_1}{d}; \quad v = 0 \quad \text{at } r = \frac{R_2}{d} \quad \text{and} \quad (4)$$

$$0 < z < \frac{L}{d}.$$

The equations are spatially discretized by means of the finite element method. The elements are second-order quadrangles (9 nodes) for the velocities and linear ones (4 nodes) for the pressure. Thus the velocity gradients and the vorticity are obtained within a linear approximation. Nevertheless, there is a discontinuity of v in the corners at the inner cylinder. This problem was overcome by imposing a zero velocity at the first and last nodes of the inner boundary discretization.

The resulting non-linear discrete system is formulated in Arrow-Hurwics's approach:

$$-\frac{1}{Re} \Delta \vec{u} + (\vec{u} \cdot \vec{\nabla}) \vec{u} + \vec{\nabla} p = \vec{f}$$

$$\frac{\partial p}{\partial t} + \rho \vec{\nabla} \cdot \vec{u} = 0.$$

Due to the convective term we use an iterative method which turns the system in hand into a sequence of Stokes's problems in which the right-hand side is changed at each iteration. The process leads to a sequence of approximate solutions u^0, u^1, \dots, u^n , given by the system:

$$-\frac{1}{Re} (\Delta \vec{u})^{n+1} + (\vec{\nabla} p)^n = \vec{f}^{n+1} - (\vec{u}^n \cdot \vec{\nabla}) \vec{u}^n$$

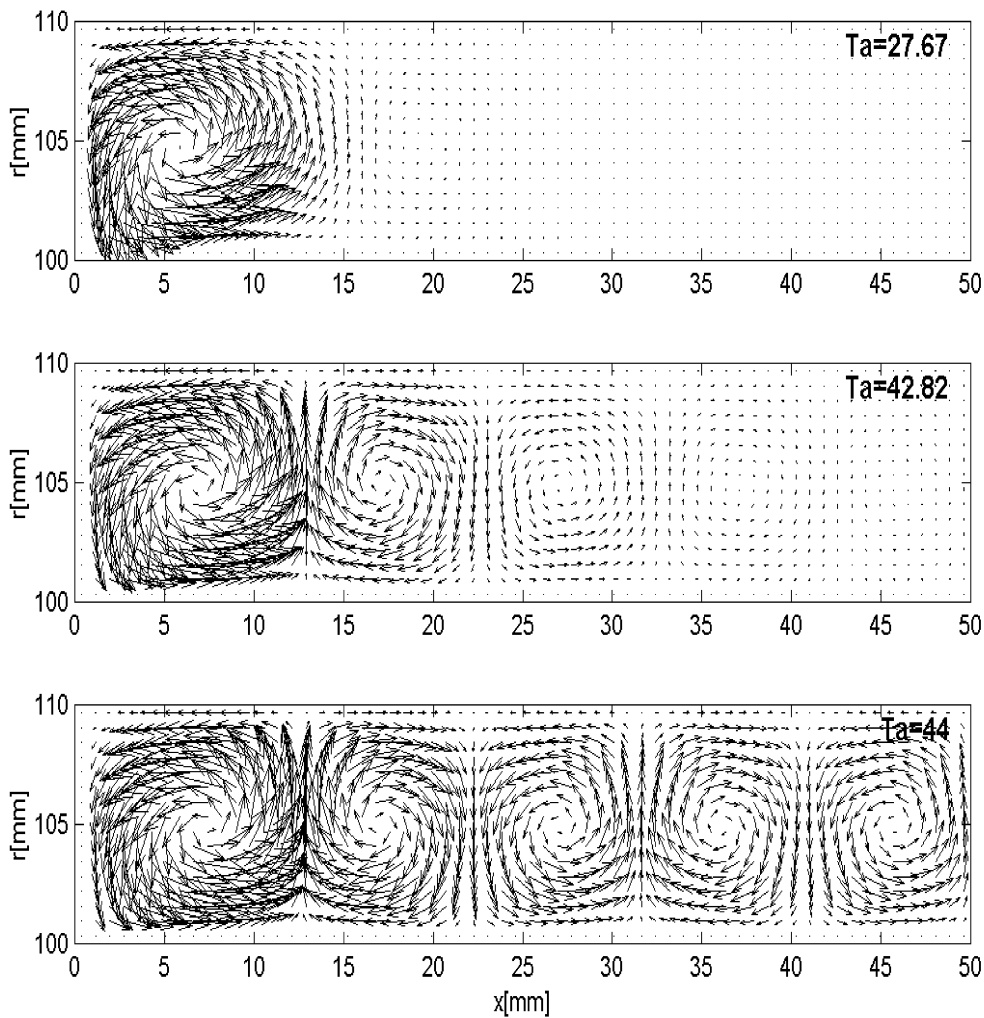


Fig. 9. Dependence of the secondary flow on the Taylor number. At $Ta = 27.67$ ($\mu = 48 \text{ mPa s}$, $\Omega = 4 \text{ rad s}^{-1}$) only the Ekman vortex is present (upper figure). At $Ta = 42.82$ ($\Omega = 6.19 \text{ rad s}^{-1}$) Taylor vortices are born (middle figure) and at $Ta = 43.99$ ($\Omega = 6.36 \text{ rad s}^{-1}$) Taylor vortices are developed (lower figure).

$$\frac{p^{n+1} - p^n}{k} + \rho(\vec{\nabla}\vec{u})^{n+1} = 0.$$

The time step is denoted by k and the couple (\vec{u}^0, p^0) is a first estimate; the best one being the Couette solution. We use the Lagrangian method for the resolution of the system. Indeed, it is efficient for quadratic problems with linear constraints. Among all tested algorithms, we retained the conjugate gradient whose parameters can be chosen automatically. The convergence of these methods is linear. The final algebraic systems are solved by means of Gauss–Seidel procedure [22].

The mesh is regular both in r and z with element size of order 0.6×0.6 mm. This is obtained with 32×256 points for the corresponding experimental geometry.

5. Results and discussion

The numerical results on the vortices development are shown in Fig. 9 in dependence on Taylor number. The velocity vectors, composed of the radial and axial components, are presented by arrows. At the lowest Taylor number, $Ta = 27.67$ ($\mu = 48$ mPa s, $\Omega = 4$ rad s^{-1}), only Ekman vortex is present in the half-gap. Theoretically it spreads until the middle of the gap where it has very low velocity. At $Ta = 42.82$ ($\Omega = 6.19$ rad s^{-1}), the Taylor vortices are born and the Ekman vortex is squeezed into a length of about 13 mm. At $Ta = 43.99$ ($\Omega = 6.36$ rad s^{-1}), the Taylor vortices are fully developed, but their intensity is smaller than the intensity of the Ekman vortex. When the Taylor vortices are present, the length of the Ekman vortex can be considered as constant.

The distribution of the velocity gradient components

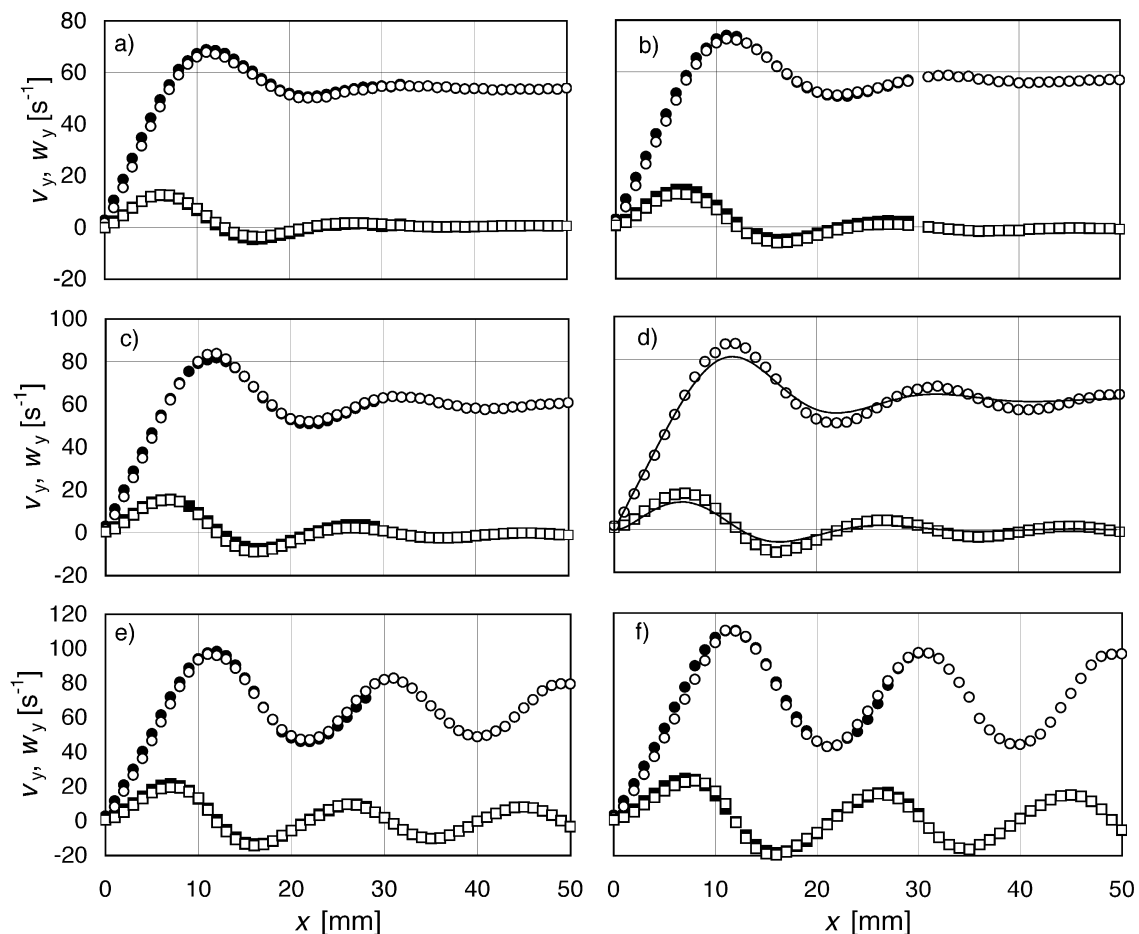


Fig. 10. Distribution of azimuthal and axial components of velocity gradient at the fixed cylindrical wall in 10-cells mode. Open points stand for probe #2, full points for probe #1, round points for $\partial v/\partial y$ and square points for $\partial w/\partial y$. $\mu = 0.048$ Pa s, $\Omega_C = 6.19$ rad s^{-1} , $\Omega/\Omega_C =$ (a) 0.93, (b) 0.96, (c) 0.99, (d) 1, (e) 1.03, (f) 1.08.

at the wall of the outer cylinder, and the values of the velocity gradient components at one point of the fixed ring which were measured by three-segment probes are shown schematically in Fig. 3.

The results measured in the Emkarox solution with a viscosity of 48 mPa s are shown in Fig. 10. The distance x spreads only into half-length of the gap. With the aim of comparing the function of the electrodes in the wall, the data are shown on this half-length. As $\partial w/\partial y$ is an odd function of z , one series was taken with the opposite sign. The data measured by the probes coincide within a limit of 5%.

As confirmed by the numerical simulation, the Ekman vortices are present at small rotation rates (Fig. 10(a)). At higher rotation rates, but which are still smaller than that corresponding to the critical Taylor number, slowly rotating cells appeared between the Ekman cells (Fig. 10(b) and (c)). At supercritical rotation rate (Fig. 10(d) and (f)), the flow in these cells was more important but the amplitudes of velocity gradients never reached those of the Ekman vortices. Maximum and minimum values of the velocity gradient components are given in Table 1. Regardless of whether the cylinder rotation was started slowly or abruptly, 10 cells always developed in the gap.

The flow of the more dilute Emkarox solution (a vis-

cosity of 21 mPa s) is sensitive to the starting process. To obtain 10 cells, it was necessary to slowly increase the rotation rate. These results are shown in Fig. 11 and Table 1. The amplitudes of the Ekman vortices were still greater than the amplitudes of the inner vortices. Higher normalized rotation rates Ω/Ω_C which were achieved with this lower viscosity solution resulted in a skew axial dependence of $\partial w/\partial y$ on z . The changes of this component were steeper at sources (maximum of the azimuthal velocity gradient component) than in sinks. In other words, the extremes of $\partial w/\partial y$ were closer to source than to sink. The distribution of $\partial v/\partial y$ was still symmetric with almost constant values of minima in sinks dependent only on rotation rate. When the rotation rate was set-up abruptly to a value superior to the critical rate, 12 cells are accommodated in the apparatus (Fig. 12). This number of cells remained constant even if the rotation rate was slowed down to the critical value. The regime with 8 cells occurred once in this solution. Comparison of the wall velocity gradient components for 8, 10 and 12 cells is shown in Fig. 13. The amplitude of the Ekman vortex increases slightly with decreasing number of cells, or in other words with increasing length of the Ekman cell.

The dependence of the maximum and minimum of

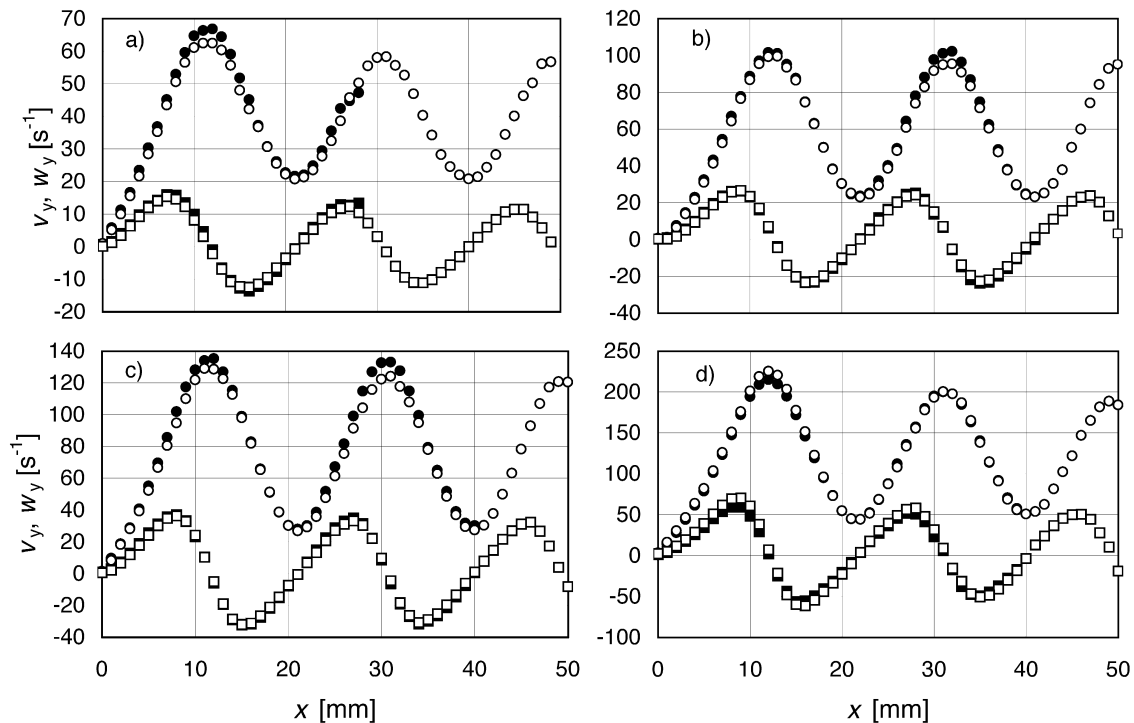


Fig. 11. Distribution of azimuthal and axial components of velocity gradient at the fixed cylindrical wall in 10 cells mode: $\mu = 0.0227$ Pa s, $\Omega_C = 3$ rad s^{-1} , $\Omega/\Omega_C =$ (a) 1.12, (b) 1.30, (c) 1.47, $\mu = 0.0214$ Pa s, $\Omega_C = 2.83$ rad s^{-1} , $\Omega/\Omega_C =$ (d) 2.

Table 1

Extremes of azimuthal and axial components of velocity gradients for 10 cells mode in two EMKAROX solutions^a

c_E	μ, ρ	Ω_c, Ω_w	Ω	$v_{y, \text{extr}}/x, w_{y, \text{extr}}/x$						$v_y, \text{Couette}$	
20%	48×10^{-3} 1050	6.19	5.66	68.3/11	50.3/22					53.7/49	53, 9
				12.6/6	-4.2/16						
					5.83	73.3/11	50.7/22	58.6/33	55.6/40	56.3/49	55, 5
						13.6/6	-5.5/16	1.6/28			
					6.01	82.7/12	51.4/22	63.7/31	58.2/40	60.4/49	57, 2
						15.7/7	-8.0/16	3.0/26	-2.4/36		
					6.19	86.9/12	49.6/22	67.3/32	56.2/40	63.2/49	59, 0
						17.1/7	-10.4/16	4.8/27	-3.4/36	1.5/45	
					6.36	97.4/12	46.5/22	82.8/31	48.8/40	79.5/49	60, 6
						20.6/7	-14/16	9.6/27	-10.2/35	8.2/45	
				6.54	110/11	42.9/21	96.8/30	44.1/40	96.1/49	62, 3	
					23.8/7	-19/16	16.0/27	-16.3/35	15.0/45		
14.3%	22.7×10^{-3} 1040	3	3.35	64.6/12	21.2/21	59.5/31	20.8/40	56.7/49		31, 9	
				15.6/7	-13/16	12.8/27	-11.1/35	11.4/45			
					3.89	100/12	23.3/21	98.8/31	23.1/40	95.2/49	37, 0
						26.4/7	-23.3/15	24.7/27	-23.2/34	23.1/45	
					4.42	132/12	27.3/21	128/31	28.5/40	121/49	42, 1
						36.6/8	-32.3/15	34.0/27	-31.2/34	32.2/46	
					2.83	220/12	44.3/22	200/31	51.2/40	188/49	53, 9
						65.5/8	-59.0/15	54.9/27	-50.0/35	50.4/45	
		21.4×10^{-3} 1039									

^a x denotes distance from ring in millimeters (Fig. 1).

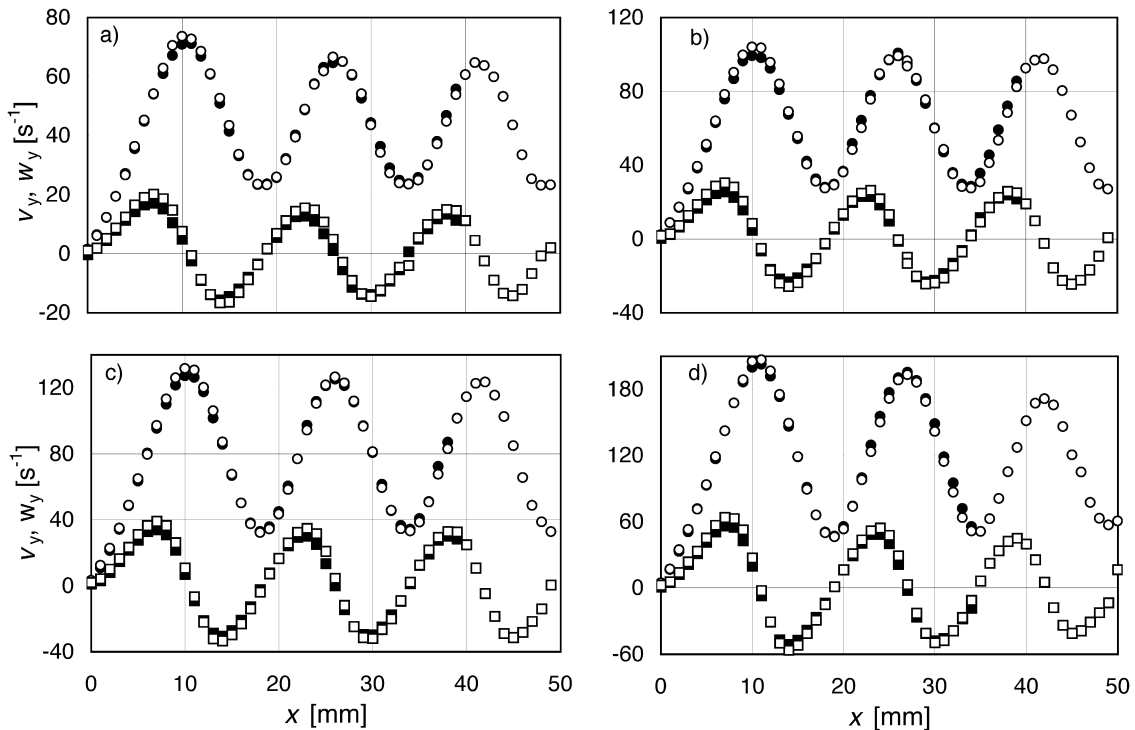


Fig. 12. Distribution of azimuthal and axial components of velocity gradient at the fixed cylindrical wall in 12 cells mode: $\mu = 0.0214 \text{ Pa s}$, $\Omega_c = 2.83 \text{ rad s}^{-1}$, $\Omega/\Omega_c =$ (a) 1.19, (b) 1.38, (c) 1.56, (d) 2.

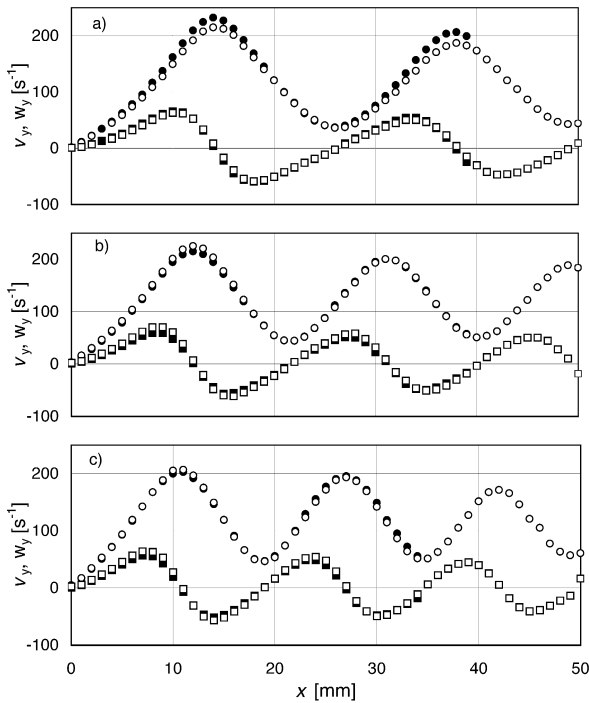


Fig. 13. Comparison of 8 (a), 10 (b) and 12 (c) cells modes: $\mu = 0.0214 \text{ Pa s}$, $\Omega_C = 2.83 \text{ rad s}^{-1}$, $\Omega/\Omega_C = 2$.

$\partial v/\partial y$ on the Taylor number is shown in Fig. 14. These values were measured in the 10-cell regime. The velocity gradient components were normalized by the wall gradient in laminar Couette flow at $Ta_c = 42.8$. Two regions can be distinguished. For $Ta < Ta_c$ the maximum grows slowly and the values are slightly greater than in laminar Couette flow. Starting with Ta_c the growth is more progressive and follows the line

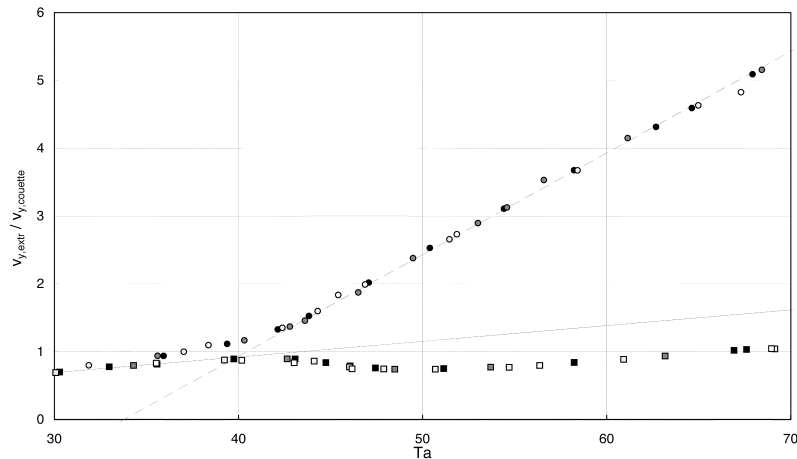


Fig. 14. Dependence of normalized maxima (circles) and minima (squares) of azimuthal component of velocity gradient on Taylor number. The shadows stand for viscosity: \square — 0.0214; \blacksquare — 0.047; \boxtimes — 0.0531; \blacksquare — 0.0663 Pa s.

$0.15Ta - 5.07$. There is a decrease in the minimum starting at Ta_c . From Ta about 48 the minimum increases slowly, but never exceeds the corresponding hypothetical value of the laminar Couette flow. An abrupt change can also be observed in the dependence of the extremes of $\partial w/\partial y$ on Taylor number (Fig. 15). As $\partial w/\partial y$ alternates along the gap, the absolute values of maximum and minimum are shown in this figure.

The velocity gradient at the fixed upper ring was measured only in one solution with a viscosity of 48 mPa s at a radial distance of 3.3 mm from the inner cylinder. The measured components $\partial u/\partial x$ and $\partial v/\partial x$ are shown in Fig. 16 against the rotation rate. The measurements are in very good agreement with the numerical simulations. At the beginning, $\partial v/\partial x$ grows almost linearly with Ω . At a low Ta , $\partial u/\partial x$ achieves small negative values. This is probably due to a little secondary counter rotating vortex in the corner of the inner cylinder, which was observed by Cliffe and Mullin [23].

6. Conclusions

This work has focused on the boundary effects on the first transition in confined circular Couette flow. The measurements accomplished by the wall shear rate probes as well as the numerical simulations made it possible to confirm the following scenario of incipience of secondary flow with increasing Taylor number. A secondary flow, so-called Ekman vortices, is always present at the fixed confining rings. Its intensity increases with the rotation rate of the inner cylinder. The next pair of vortices appears between the Ekman vortices at Ta about $0.95 Ta_c$, reducing the space occupied by the two end wall Ekman vortices. This new

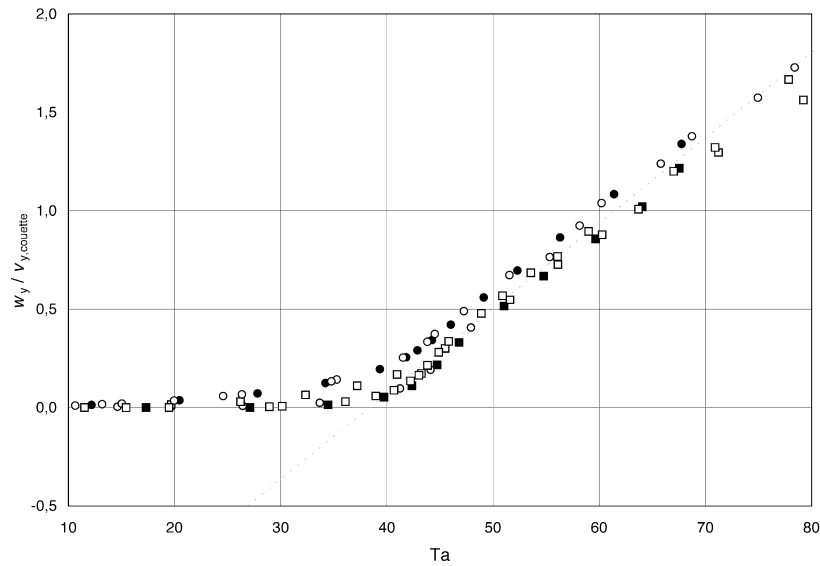


Fig. 15. Dependence of normalized maxima (circles) and minima (squares) of axial component of velocity gradient on Taylor number. The shadows stand for viscosity: □ — 0.0214; ◐ — 0.047; ▩ — 0.0531; ■ — 0.0663 Pa s.

pair is obviously related to Taylor instability, but the bifurcation differs from the classical case. This birth process is local and continues with increasing Taylor number until the whole domain is fulfilled. The final number of vortices depends on the way in which the rotation rate was adjusted.

At Ta_c the maximum value of $\partial v / \partial y$ in the Ekman vortex is 1.44 times greater than the gradient in laminar Couette flow. For $Ta > Ta_c$ these maxima grow linearly with Ta .

The extremes of $\partial w / \partial y$ and $\partial v / \partial y$ are only slightly dependent on the cell number. To a first approximation, these extremes normalized by the velocity gradient at the critical laminar Couette flow depend only on Taylor number.

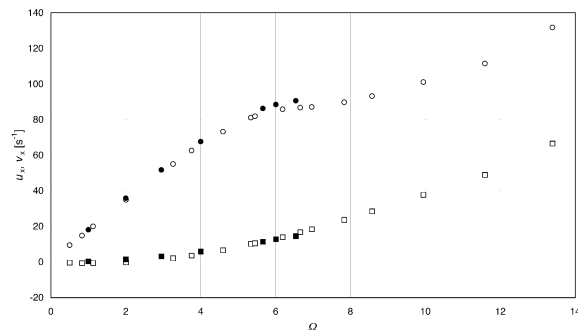


Fig. 16. Dependence of normalized velocity gradient components at the fixed ring on Taylor number circles — $\partial u / \partial x$, squares — $\partial v / \partial x$, open points — measurements, full points — numerical simulations.

The minima of $\partial v / \partial y$ have local minimum approximately at $Ta = 50$ (which is slightly higher than Ta_c), then grow with Ta and approach the hypothetical value of velocity gradient in laminar Couette flow.

The measured distribution of the components of the velocity gradient can be used for verifying computational fluid dynamics software.

The metallic bands which connect the upper and lower rings do not interfere with the flow.

The Emkarox solutions with concentrations used in our experiments do not exhibit elasticity which would lower the critical Taylor number.

Acknowledgements

This work was supported by a fellowship 'Haut niveau' of MENESRIP France (V.S.) and by the European project COST F2 'Electrochemical sensors for flow measurements' granted by the Czech Republic.

The authors express their thanks to ICI, Frankfurt, Germany, which donated the polyalkylen glycols EMKAROX HV45 and to the United Chemical and Metallurgical Works, Ltd., Ústí n. L., Czech Republic, which donated the resins Epoxy 1200 and CHS 521.

References

- [1] R. Tagg, in: C.D. Andereck, F. Hayot (Eds.), *A Guide Literature Related to the Couette–Taylor Problem in Ordered and Turbulent Patterns in Taylor–Couette Flow*, Plenum Press, New York, 1992, pp. 303–357.

- [2] J. Legrand, F. Coeuret, Circumferential mixing in one-phase and two-phase Taylor vortex flows, *Chem. Engng. Sci.* 41 (1986) 47–53.
- [3] G. Desmet, H. Verelst, G.V. Baron, Local and global dispersion effects in Couette–Taylor flow — II. Quantitative measurements and discussion of the reactor performance, *Chem. Engng. Sci.* 51 (1996) 1299–1309.
- [4] K. Kataoka, N. Ohmura, M. Kouzu, Y. Simamura, M. Okubo, Emulsion polymerization of styren in a continuous Taylor vortex flow, *Chem. Engng. Sci.* 50 (1994) 1409–1416.
- [5] P. Mikulasek, Methods to reduce concentration polarization and fouling in membrane filtration, *Collect. Czech. Chem. Commun.* 59 (1994) 737–755.
- [6] E. Dumont, Caractérisation des écoulements et des frottements pariétaux dans un échangeur de chaleur à surface raclée, Ph.D. Thesis, Univ. Nantes, France, 1999.
- [7] C.D. Andereck, S.S. Liu, H.L. Swinney, Flow regimes in a circular Couette system with independently rotating cylinders, *J. Fluid Mech.* 164 (1986) 155–183.
- [8] T.B. Benjamin, Bifurcation phenomena in steady flows of a viscous liquid. Part I: Theory, *Proc. R. Soc. Lond. A* 359 (1978) 1–26.
- [9] T.B. Benjamin, Bifurcation phenomena in steady flows of a viscous liquid. Part II: Experiments, *Proc. R. Soc. Lond. A* 359 (1978) 27–43.
- [10] T. Mullin, Mutations of steady cellular flows in the Taylor experiment, *J. Fluid Mech.* 121 (1982) 207–218.
- [11] K.A. Cliffe, Numerical calculations of the primary-flow exchange process in the Taylor problem, *J. Fluid Mech.* 197 (1988) 57–79.
- [12] M.E. Anadouli, Etude des instabilités imparfaites de Couette Taylor, Ph.D. Thesis, Institut National Polytechnique de Lorraine, Nancy, France, 1994.
- [13] G. Cognet, Utilisation de la polarographie pour l'étude de l'écoulement de Couette, *J. Mécanique* 10 (1971) 65–90.
- [14] V. Sobolík, Electrochemical study of Couette–Taylor flow by limiting diffusion current method, *Collect. Czech. Chem. Commun.* 64 (1999) 1193–1210.
- [15] A. Ait Aider, Séquences transitoires en écoulement de Couette–Taylor, Influence du rapport d'aspect, Ph.D. Thesis, INPL, Nancy, 1983.
- [16] L. Choplin, P.J. Carreau, A. Ait Kadi, Highly elastic-constant viscosity fluids, *Poly. Engng. Sci.* 23 (1983) 459–464.
- [17] R.H. Thomas, K.W. Walters, The stability of elastoviscous flow between rotating cylinders — Part I, *J. Fluid Mech.* 18 (1963) 33–43.
- [18] D.C. Di Prima, H.L. Swinney, Instability and transition in flow between concentric rotating cylinders, in: *Topics in Applied Physics*, vol. 45, Springer-Verlag, Berlin, 1981, pp. 139–180.
- [19] O. Wein, V. Sobolík, Theory of direction sensitive probes for electrodiffusion measurement of wall velocity gradients, *Collect. Czech. Chem. Commun.* 52 (1987) 2169–2180.
- [20] O. Wein, V. Sobolík, EDWORK91 Manual, Technical Report, Institute of Chemical Process Fundamentals, Prague, 1992.
- [21] C. Deslouis, O. Gil, V. Sobolík, Electrodiffusional probe for measurement of the wall shear rate vector, *Int. J. Heat Mass Transfer* 33 (1990) 1363–1366.
- [22] M. Fortin, R. Peyret, R. Temam, Résolution numérique des équations de Navier–Stokes pour un fluide incompressible, *Journal de Mécanique* 10 (3) (1971) 357–390.
- [23] K.A. Cliffe, T. Mullin, A numerical and experimental study of anomalous modes in the Taylor experiment, *J. Fluid Mech.* 153 (1985) 243–258.